Feasibility of particle image velocimetry for low-speed unconventional vapor flows

Head, A. J.; Colonna, P.; Schrijer, F.; Gallo, M.; Novara, M.

DOI
10.1016/j.expthermflusci.2018.10.028

Publication date
2019

Document Version
Final published version

Published in
Experimental Thermal and Fluid Science

Experimental Thermal and Fluid Science 102 (2019) 589–594

Contents lists available at ScienceDirect

Experimental Thermal and Fluid Science

journal homepage: www.elsevier.com/locate/etfs

Feasibility of particle image velocimetry for low-speed unconventional vapor flows

A.J. Head[a], M. Novara[d], M. Gallo[c], F. Schrijer[b], P. Colonna[a,*]

[a] Propulsion & Power, Aerospace Engineering, Delft University of Technology, Kluyverweg 1, 2629 HS, Delft, The Netherlands
[b] Aerodynamics, Aerospace Engineering, Delft University of Technology, Kluyverweg 2, 2629 HS, Delft, The Netherlands
[c] Aeronautical Engineering, Inholland University of Applied Sciences, Rotterdamseweg 141, 2628AL Delft, The Netherlands
[d] Institute of Aerodynamics and Flow Technology, DLR, Göttingen, Germany

ARTICLE INFO

Keywords:
Siloxane fluids
Low speed rotating organic vapor flow
Particle image velocimetry
Seeding technique

ABSTRACT

This work assesses the feasibility of the planar PIV technique to study the characteristics of a siloxane vapor D_4. Titanium dioxide (TiO_2) seeding particles were used to track the motion around a rotating disk in a low speed flow. Vector fields of natural convection (NC) and a superposition of NC and rotating flow were selected as exemplary cases. The particles were capable of tracing the flow since the calculated Stokes number St is 6.5×10^{-5}. The quality of the experimental data is assessed by means of particle seeding density and particle image Signal to Noise ratio (S/N). The final results are deemed acceptable for an accurate assessment of the flow field. Rejected outliers are below 2.3% and the relative uncertainties corresponding to the average velocity fields are below 1%.

1. Introduction

Organic compounds are used as working fluids in many power and refrigeration applications, such as organic Rankine cycle (ORC) and supercritical carbon dioxide power systems, vapor compression cycle systems, and in other chemical, and transport processes. In many of these processes, flows occur in the non-ideal compressible fluid dynamic (NICFD) regime at high relative pressure and temperature [4]. The fluid dynamic design of machinery operating in these conditions necessitates validated CFD codes. Validation can be performed only if accurate experimental information covering a representative range of conditions is available. Particle image velocimetry (PIV) is arguably the experimental technique of choice for providing these data. Some initial attempts of using PIV in this type of flows are documented in [10,14]. The investigation described here aims at addressing some of the issues related to utilizing PIV in high-temperature organic vapors moving at low speed. This work serves also as a precursor study before performing PIV in transonic and supersonic flows of organic fluids in a newly built experimental facility [5].

2. Optical properties and particle compatibility

PIV measurements require a transparent fluid, i.e., laser light absorption should be insignificant. In addition, ideally, the index of refraction should remain constant, such that aero-optical aberrations are minimal [3]. The refractive index n and the extinction coefficient k characterize how light propagates through a medium. With regards to members of the siloxane family, e.g., MM and D_4, these parameters are not available for the vapor state because measurements of reflectance, transmittance or ellipsometric parameters are not documented. However, the refractive index can be estimated from measurements of the molar refractivity

$$A = \frac{4\pi}{3} N_A \alpha,$$

together with the Lorentz-Lorenz formula

$$\alpha = \frac{3}{4\pi N} \frac{n^2 - 1}{n^2 + 2},$$

and the molar volume

$$V_m = \frac{N_m}{N} = \frac{M}{\rho}.$$

This results in an explicit equation relating the refractive index to the density of the medium, namely

$$n = \sqrt{\frac{2A_s\rho + 1}{1 - A_s\rho}},$$

* Corresponding author.
E-mail address: P.Colonna@tudelft.nl (P.,. Colonna, >.

https://doi.org/10.1016/j.expthermflusci.2018.10.028
Received 17 April 2018; Received in revised form 22 October 2018; Accepted 24 October 2018
Available online 02 November 2018

Nomenclature

ω	angular velocity [rad sec^{-1}]
ρ	density [kg m^{-3}]
$\phi_{fg}(m, n)$	(normalized) cross-correlation coefficient[–]
μ	viscosity [kg s^{-1} m^{-1}]
β	volumetric thermal expansivity [K^{-1}]
α	thermal diffusivity [–]
Q	average correlation peak ratio [–]
N_A	Avogadro's number [mol^{-1}]
H	characteristic thickness of fluid layer [m]
Z	compressibility factor [–]
k	extinction coefficient [–]
M	molar mass [kg mol^{-1}]
A	molar refractivity [cm^3 mol^{-1}]
V_m	molar volume [m^3 mol^{-1}]
d_p	particle diameter [m]
u_{pr}	particles' radial velocity [m s^{-1}]
Re_p	particle Reynolds number [–]
u_{tr}	particles' tangential velocity [m s^{-1}]
Ra	Rayleigh number [–]
n	refractive index [–]
C_p	specific heat at constant pressure [J kg^{-1} K^{-1}]
k	thermal conductivity [W m^{-1} K^{-1}]

where N_A is Avogadro's number, N is the number of molecules per unit volume, and

$$A_s = \frac{A}{M}$$

is the specific refractivity, with M being the molar mass. If measurements of the molecular refractivity are unavailable then A may be estimated by the concept of *additivity of bond refractions* and by simplified methods given by Warrick [15]. The A for D_4 is calculated as 74.5 cm^3 mol^{-1} which results in a similar index of refraction value if compared to that of air at low density; namely, ≈ 1 and therefore no additional difficulties are expected with respect to PIV measurements. However, for high speed organic flows the density variations are larger and can change by two orders of magnitude over a short distance [5], imposing up to a 7% variation in the refractive index over the expansion path. In this case, the apparent shift (normal or lateral) or blurring (smearing) of the particle image could change substantially [2], and measures should be taken to ensure an appropriate depth of focus is selected. Absorption spectra have not been reported for organosilicon compounds in the vapor state and thus the extinction coefficient cannot be estimated. However, provided that the medium is sufficiently transparent for the particles to scatter enough light, then the particle image signal to noise (S/N) ratio, i.e., the ratio between the particle peak intensity and the image noise level, will be large enough to perform PIV measurements. If the medium is D_4, this condition is satisfied and results are discussed in Sections 4 and 5.

Particles for PIV experiments should be preferably inexpensive, non-toxic, non-corrosive, non-abrasive, non-volatile, and chemically inert. Commonly used seeding materials for high temperature flows are dry metal oxide powders, e.g., Aluminum Dioxide Al_2O_3 or Titanium Dioxide TiO_2, and Silica spheres SiO_2. However, dispersing the solid particles uniformly in a hot gas flow is challenging. Especially if the flow to be studied is formed by organic molecules, since it must not be contaminated by, e.g., water or air, as this would affect its thermal stability [7]. The introduction of solid particles by atomization of a suspension is the most viable possibility for the envisaged experiments [2].

3. The non-intrusive vapor analyser (NIVA)

PIV experiments were performed in the NIVA: organic vapour is enclosed in a vessel with optical access, and a rotating disk provides fluid motion. Fig. 1 shows the back-side view of the NIVA together with the control hardware. The setup characteristics and design specifications are listed in Table 1.

A stainless-steal (SS) cube with two borosilicate (Borofloat 33) windows is positioned on top of a heating plate (max. power 2.2 kW). The set-point temperature is controlled by a relay and a thermocouple which is located inside the bottom flange. The temperature at the top flange can be monitored with an additional thermocouple and readout device. In order to limit thermal losses, the SS cube's exterior was insulated with rockwool. The interior of the cube is air-tightened by means of a metal lid and snap-clamp. The air can be removed from the cube through a ball-valve such that the organic vapor will not be contaminated. A sheet of Viton is used as a gasket, which, in addition, serves as insulator minimizing the thermal stresses of the windows. Since the operational temperature of the Siemens Sitran P200 pressure transmitter must not exceed 145 °C, the sensor was mounted at the end of a pipe which protrudes from the lid. This allows for monitoring the pressure inside the cube. Furthermore a safety blow-off valve is installed to ensure that the maximum operating pressure cannot be exceeded. A 0–50 Hz (0–2800 RPM) frequency controller modulates a 0.18 kW electric motor, which connects to a 100 mm circular flat disk (located inside the cube and visible in the top-right of Fig. 2) via a flexible shaft coupling. The shaft is sealed with a Viton o-ring and is situated in a bearing holder. The inverter frequency and corresponding disk rotation was checked directly using an optical approach. A

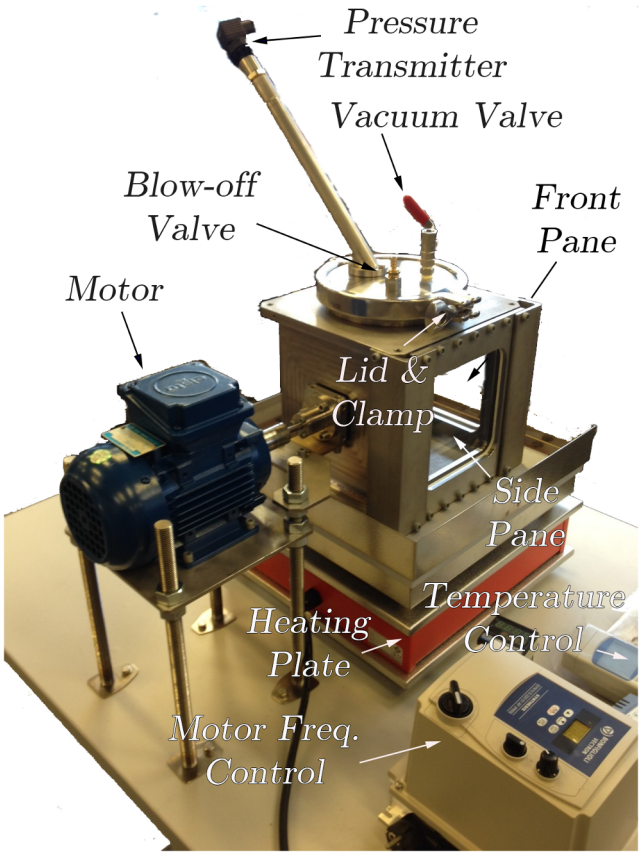

Fig. 1. The NIVA Apparatus.

Table 1
Characteristics of the experiment.

NIVA Apparatus		
Design Pressure	$P_{max,abs}$	2 bar
Design Temp	T_{max}	180 °C
Motor	ω_{max}	2800 RPM
Disk Diameter	D	0.1 m
Inner Box Dimensions	$L \times H \times W$	0.178 × 0.178 × 0.178 m
Glass Dimensions	$L \times H \times W$	0.15 × 0.015 × 0.015 m
Wall thickness	t	0.01 m
Imaging and Illumination		
Magnification Factor	M	0.19
fstop	$f_{\#}$	4
Thickness of the light sheet	t	1 mm
Focal length of lens	f	60 mm
Particle image diameter	d_τ	3 pixels
Depth of Focus	δZ	1.6 mm
Laser pulse separation	$\Delta t = 1/f_{acq}$	0.003 s

reference point was imaged at the edge of the rotating disk at several different time instances for a specific inverter control frequency, e.g., 10, 20 … 50 Hz. Knowing the Δt between images, e.g., 1000 µs, with a fixed distance from the center of the disk, one could estimate the tangential velocity and rotational speed. The corresponding maximum tangential velocity at the edge of the disk is 15 m/s. The inside of the cube, together with the disk, was painted matt black in order to limit laser light reflections.

Fig. 2 shows the layout of the PIV system. A high speed camera (Imager Pro 4M) with pixel size of 11 × 11 µm and a Nikkor lens is used to record the particle images. Illumination is provided by a Litron LDY300 (Nd:YLF) laser. Furthermore a LaVision high speed controller is used to synchronize the camera, laser and data acquisition PC. An exploded isometric view of the NIVA shows the location of the measurement plane, which is situated 10 mm from the surface parallel to the disk. This distance was chosen as a trade-off between laser light reflections and identifying phenomena induced by the disk, e.g., the closer the measurement plane the easier it was to capture the flow vortices but resulted in more background noise due to the surface of the rotating disk. The field of view (FOV) is 0.12 m × 0.12 m and is large enough to capture the flow rotating with and around the disk. The cross-correlation analysis of the image-pairs was done with the LaVision Davis software version 8.3.0 and data post processing was conducted with MATLAB. Sequences of 1000 images were acquired, which, at the 300 Hz acquisition frequency in single frame mode, results in a total acquisition time of 3.3 s. The seeding material was TiO_2, with a primary crystal size of 0.17 µm (CAS No. 13463-67-7) and effective bulk density of $\rho = 10^3$ kg/m^3 [9], since it is a typical choice for high temperature flows. A larger primary crystal size of 0.30 µm was also used in the experiments but resulted in larger particle agglomeration and a less even seeding distribution. Table 1 further summarizes all the primary characteristics of the imaging and illumination system.

Experiments were conducted in siloxane D_4 at an average temperature of 160 °C and 0.283 bara. The amount of working fluid was determined based on the requirement that the temperature of the experiment cannot be larger than 180 °C, which is constrained by the operation of pressure safety valve and pressure transmitter. Given that at ambient temperature the quantity of fluid in the vapor phase is negligible, the amount of liquid is determined by the smallest density achievable at that temperature. The fluid charge is therefore 20 ml.

In order to determine if the particle velocity accurately represents the fluid velocity, a simplified situation of forced vortex flow is considered, whereby the particle dynamics is governed by simple rotational motion. It is reasonable to neglect the tangential and radial acceleration – similarly to what is typically done for many centrifugal filters – especially in cases where particles have reached the tangential fluid velocity, and the particles' radial velocity is comparatively small. Additionally, if it is assumed that the spherical particles move according to Stokes' law, then the centrifugal and Stokes' force can be equated, from which the particles' radial velocity becomes

$$u_{pr} = \frac{r\omega^2 d_p^2 \rho_p}{18\mu}.$$

This expression is valid for small particles with Reynolds numbers

$$Re_p = \frac{\rho_f u_{pr} d_p}{\mu} < 1,$$

such that the flow around the particle is within the Stokes regime [2]. ρ_p and d_p are the particle density and diameter, respectively. Thermophysical properties of D_4 are calculated by means of a library [1] implementing a variety of models, e.g., the thermodynamic and transport property values are calculated by using the iPRSV equation of state [13] and Chung's model, respectively. μ is the viscosity (equal to 7.7×10^{-5} kg s^{-1} m^{-1} in the experimental conditions defined above), and r is the characteristic dimension of the disk. Considering the particles' radial velocity as defined above, then Re_p is lower than one, and together with the tangential velocity $u_{tp} = r\omega$, where ω is the angular

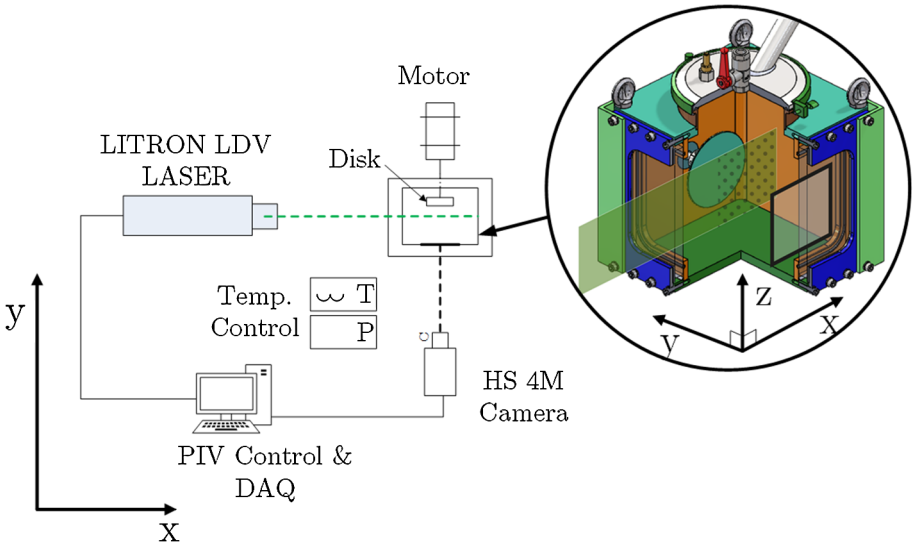

Fig. 2. The layout of the system.

velocity, then

$$\frac{u_{\mathrm{rp}}}{u_{\mathrm{tp}}} = \frac{\omega d_p^2 \rho_{\mathrm{p}}}{18\mu}$$

equals 6.5×10^{-5}. This is similar in form to Stokes' law, as reported by Lapple and Shepherd [6], but for simple rotational motion. Given that the tangential component dominates, it can be inferred that the chosen particles are suitable for accurately tracing the motion of the flow around the disk.

4. Experimental procedure

A 20 ml suspension of D_4 and TiO_2 particles was prepared at room temperature and subsequently poured over the bottom of the cubic vessel. Then the chamber was sealed by affixing the lid to the vessel and by tightening the quick-release-clamp. Air was extracted via the ball-valve, with a vacuum pump. The final vacuum pressure was 5 mbar and monitored for approx. 1 h to ensure that the container was leak tight. The vessel was then insulated with rockwool, and then the thermal control was initiated. In the meantime, the actuator disk was set to rotate anticlockwise at 10 Hz (600 RPM) in order to provide some forced convection inside the vessel during the phase transition. Without forced convection most of the particles tended to settle on the bottom of the container, thus their density in the vapor would be insufficient to perform PIV measurements.

The evaporation process can be seen in Fig. 3. During the heating, a turbulent convective circulation establishes, whereby the suspension moves upward due to the heating from the bottom, and then the vapor condenses due to the lower temperature of the upper surface of the box, and sizable droplets fall to the bottom. Once the fluid was completely vaporized, the required control speed of the disk was set, insulation removed and then images acquired.

The amount of particles required to provide sufficient seeding was chosen on the basis of the vector validation procedure together with observations of particle deposition inside the cube. In the initial stages of phase transition there were large agglomerates of particles at the bottom of the vessel, and the top was predominately occupied by vapor. Towards the end of the evaporation process an almost homogeneous particle distribution was attained. However, in a small layer right above the bottom, the particle density was notably lower as can be seen in Fig. 3(c). This might either be explained by an uneven illumination or an unfavorable temperature gradient between the bottom and the ceiling of the container, resulting in a higher out-of-plane particle motion. Despite the precautions taken with the insulation, thermal losses from the system resulted in a temperature at the bottom plate of 180 °C and approx. 140 °C at the ceiling.

An average particle peak intensity of 80 counts was measured, and this can be attributed to the low intensity of the laser. The corresponding average noise level was 25 counts. At the top right of the FOV, particles appear out-of-focus, see for example Fig. 3(b). These particles are illuminated by the light reflected by surfaces inside the vessel, thus they do not reside on the measurement plane. In any case, it appears that the design of the container is suitable for performing measurements with sufficient contrast.

No noticeable particle or laser light compatibility issues were observed, and the vapor turned out to be sufficiently transparent to conduct PIV. In summary, no beam dispersion due to the density of the media occurred, and the laser light propagated with negligible absorption. In order to assess the quality of the measurements, an analysis of the instantaneous and average vector fields was conducted.

5. Exemplary flow fields

Several experimental runs, corresponding to disk rotations of 10 Hz (600 RPM), 20 Hz (1280 RPM), 30 Hz (1900 RPM) and 40 Hz (2500 RPM), were carried out. Two cases were considered for the present investigation. In the first set of experiments the rotational frequency of the disk was set to 40 Hz. In the second, the disk was kept still, and the motion of the fluid was due to natural convection (NC) alone.

The preprocessing method of Mendez et al. [8] was used to improve the image quality of the raw data before it was processed with a cross-correlation technique. This is accomplished by removing the background noise, i.e., unsteady and non-uniform reflections originating from the surface of the disk, which is correlated and well approximated by the first Proper Orthogonal Decomposition (POD) modes of the image sequence. Background noise was satisfactorily removed without an appreciable alteration of the particle image brightness.

During the processing stage, the multi-grid window deformation cross-correlation technique of Scarano and Riethmuller [11,12][11] was adopted for all datasets. A final window size of 24 × 24 pixels (Gaussian weighted) with 75% overlap was selected, yielding a vector spatial resolution of 1.4 mm. The universal outlier detection approach of Westerweel and Scarano [16] was used to identify invalid vectors. Discarded vectors were replaced with a distance-weighted average of valid neighbor vectors.

5.1. Rotating disk

Fig. 4(a) shows the time-averaged vector field resulting from an anticlockwise disk rotation of 2500 RPM. The flow field is a non-linear superposition of an Ekman-type structure, originating from the constant forcing motion of the disk, and a Rayleigh-Bénard type flow. In order to assess the quality of the data, instantaneous flow fields were analysed at several instances. The average correlation peak ratio Q was 2.2, whereby $Q = \frac{P1 - \min(P)}{P2 - \min(P)}$, with P1 and P2 being the heights of the first and second highest correlation peaks, while $\min(P)$ is the lowest value of the correlation plane. The image seeding density was 0.02 particles per pixel (ppp) and corresponds to approximately 12 particles in the final window size. The seeding concentration could be increased if a

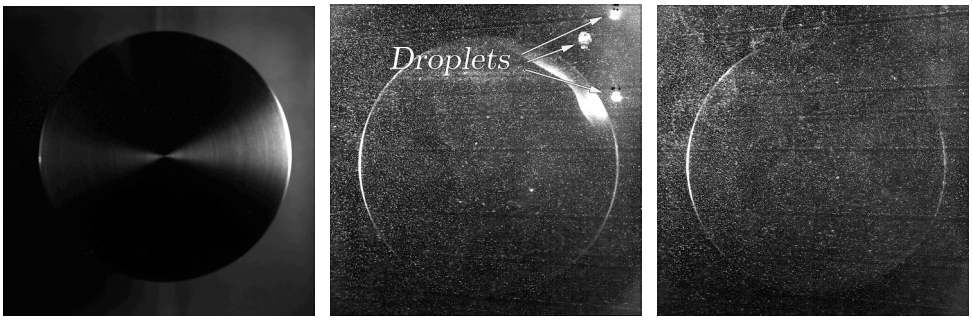

(a) All liquid (b) Droplet formation (c) All vapor

Fig. 3. Evaporation process and seeding distribution.

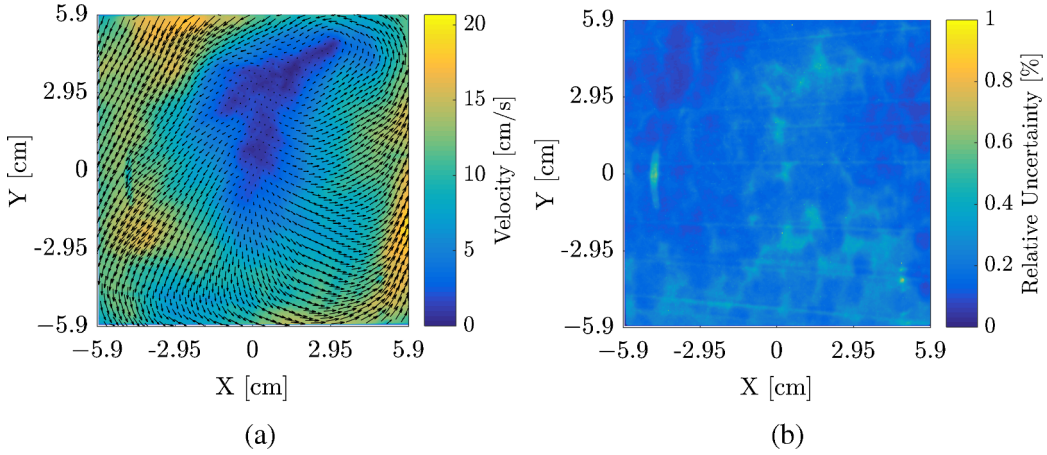

Fig. 4. Rotating at 2500 RPM (a) avg. vel. field (b) relative uncertainty.

higher spatial resolution were of interest. The (normalized) cross-correlation coefficient is defined as follows [18,12],

$$\phi_{fg}(m, n) = \frac{\sum_{i,j=1}^{M} f(i,j)\cdot g(i-m, j-n)}{\sqrt{\sum_{i,j=1}^{M}[f(i,j)]^2 \cdot \sum_{i,j=1}^{M}[g(i,j)]^2}}$$

where f and g denote the grey intensity distributions of the interrogation areas and M is the window size (in pixels). Cross-correlation values of 0.8 are observed, where values near one indicate that many particle images match up with their corresponding shifted partners. However, there were lower values in the FOV (approximately 0.5) which originate from the combined forcing motion of the disk together with the uneven thermal gradient, effectively promoting out-of plane particle movement.

As the rotation increases, the pumping force increases the loss of particle pairs. The percentage of outlier vectors which were removed is 2.3%. The flow conditions inside the cube made it difficult to obtain vector field images with a smaller number of outlier vectors. The other experimental runs which were made at different disk rotational speeds showed that the number of outliers decreased with decreasing disk speed. This can be explained by the fact that out-of plane particle motion is more prominent for higher rotational speeds.

5.2. Natural convention

Fig. 5(a) shows the averaged vector field with the disk standing still. In this case, 1 image every 20 images was processed, resulting in an effective acquisition frequency of 15 Hz. The average Q of the instantaneous fields is 2.6, somewhat larger than in case of rotating disk. The c reaches a value of 0.9, and is higher than what was estimated for the rotating disk case, because the particles maintained the in-plane motion due to the absence of the pumping effect. The image seeding density of the FOV is 0.025 ppp, giving an average of 13 particles per window. The seeding concentration is even more inhomogeneous (larger concentration at the top) compared to the rotating disk case, also because of the absence of forcing, thus particles were convected upwards. The number of outliers that were removed was 0.7%. The NC, originating from the base of the cube, together with the thermal losses from the sides, which progressively increases towards the top (increase in metal surface area), promote an acceleration of the fluid towards the ceiling. When a colloidal suspension is subjected to a temperature gradient, the dispersed particles display a drift velocity toward the colder regions in addition to the Brownian motion.

The NIVA can be approximated by a case of horizontal convection heated from the bottom with a uniform temperature profile distribution, occurring within an enclosure. The relative importance between the effects of the buoyancy forces, and the effects of the viscosity forces and thermal conduction can be assessed with the Rayleigh number. Under the assumption of infinite horizontal plates the critical value is 1708, above which natural convection initiates. The Rayleigh number is defined as

$$Ra = \frac{g\cdot\beta}{\mu\cdot\alpha}\cdot\Delta T\cdot H^3$$

where g is the gravitational acceleration and μ is the dynamic viscosity. $\Delta T = T_s - T_\infty$ is temperature difference between the surfaces of the

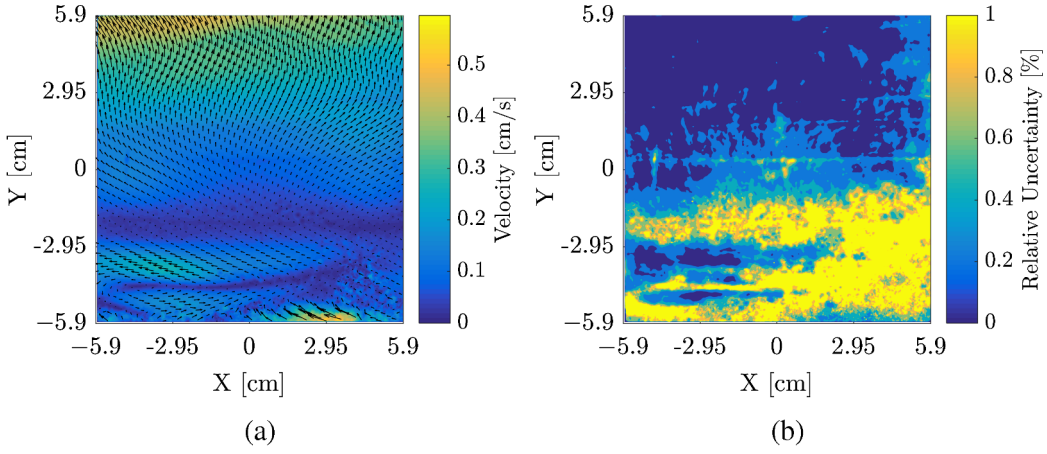

Fig. 5. NC case (a) avg. vel. field (b) relative uncertainty.

bottom and top plate. For an ideal gas with pressure held constant, the volumetric thermal expansivity (i.e. relative change in volume due to temperature change), β is the inverse of temperature. The properties of fluid are taken at an absolute pressure P of 0.283 bara and at an average temperature T inside the cube, e.g., $(T_s + T_\infty)/2$. Therefore, for natural convection from a horizontal plate, given the experimental conditions above, $\beta = 1/T = 0.00231$. This assumption is validated by calculating the compressibility factor,

$$Z = \frac{P}{\rho \cdot R/M \cdot T},$$

for the conditions inside the cube, which results in approximately 0.98. R is the universal gas constant and M the molar mass. H is the thickness of the fluid layer - or characteristic length of the fluid domain. For a flat plate, H is the area (of the bottom side) of the plate divided by its perimeter $H = \frac{w \cdot l}{2(w+l)} = 0.0445$. α is the thermal diffusivity and is defined as

$$\alpha = \frac{k}{\rho \cdot C_p}$$

and is equal to 3.7×10^{-6}, where k is the thermal conductivity, ρ is the local density and c_p is the specific heat at constant pressure.

Therefore, the Rayleigh number is calculated as 3×10^6 which is larger than the criterion for the onset of natural convection.

5.3. Uncertainty quantification

The correlation statistics approach of Wieneke [17] was used to calculate the absolute and relative uncertainty in the displacement vector from the average vector field. Figs. 4(b) and 5(b) show the corresponding relative uncertainty maps. The RMS uncertainties for Rotating case are 0.7 Abs./px and 0.4% relative, while for the NC case are 0.4 Abs./px and 1% relative. The RMS absolute uncertainty is lower for the NC case due to the lower occurrence of out-of-plane particles movement. Since the particle displacement is lower and the absolute uncertainty of the particle displacement is similar for the two cases, the relative uncertainty is higher for the NC case. The relative uncertainty is higher in the layer at the bottom of the cube, also see Fig. 5(b), because of the lower particle concentration.

6. Conclusions and outlook

The work documented here allows to draw the following conclusions regarding the use of PIV in low-speed organic vapor flows:

- The D_4 vapor is sufficiently transparent to conduct PIV;
- Evaporating the fluid together with TiO_2 seeding particles allows to obtain a proper tracer distribution: an external seeder is not needed;
- A seeding density of 0.02–0.03 ppp can be achieved with limited particle agglomeration and sufficient contrast ($Q > 2.5$);
- Particles follow the flow with sufficient accuracy ($St = 6.5 \times 10^{-5}$);
- The Rayleigh number is calculated as 3×10^6 which is larger than the criterion for the onset of natural convection; and,
- The relative uncertainty is lower than or equal to 1%.

It can be inferred that PIV is feasible in low speed flows of hot organic vapors. Further work will be devoted to devising a seeding strategy that allows to perform PIV in supersonic and transonic flows in the newly built ORCHID setup [5].

Acknowledgements

The authors are grateful to H. Lakkad for his help with vector processing, to A. Sciacchitano for his guidance on UQ analysis, and to S. van Herk for the realization of the NIVA.

References

[1] P. Colonna, T.P. van der Stelt, A. Guardone, FluidProp: A program for the estimation of thermophysical properties of fluids, 2012.
[2] F. Durst, A. Melling, J.H. Whitelaw, Principles and Practice of Laser-Doppler Anemometry, Academic Press, 1981.
[3] G.E. Elsinga, B.W. van Oudheusden, F. Scarano, Evaluation of aero-optical distortion effects in PIV, Exp. Fluids 39 (2) (2005) 246–256.
[4] J. Harinck, A. Guardone, P. Colonna, The influence of molecular complexity on expanding flows of ideal and dense gases, Phys. Fluids 21 (8) (2009) 086–101.
[5] A. Head, C. De Servi, E. Casati, M. Pini, P. Colonna, Preliminary design of the ORCHID: a facility for studying non-ideal compressible fluid dynamics and testing ORC expanders, ASME Turbo Expo, GT2016-56103, 2016, p. 14.
[6] C.E. Lapple, C.B. Shepherd, Calculation of particle trajectories, Ind. Eng. Chem. 32 (5) (1940) 605–617.
[7] C. Ludovico, P. Colonna, Thermal stability of R-134a, R-141b, R-13i1, R-7146, R-125 associated with stainless steel as a containing material, Int. J. Refrig. 20 (6) (1997) 381–389.
[8] M. Mendez, M. Raiola, A. Masullo, S. Discetti, A. Ianiro, R. Theunissen, J.M. Buchlin, POD-based background removal for particle image velocimetry, Exp. Therm. Fluid Sci. 80 (2017) 181–192.
[9] D. Ragni, F. Schrijer, B.W. van Oudheusden, F. Scarano, Particle tracer response across shocks measured by PIV, Exp. Fluids 50 (1) (2011) 53–64.
[10] U. Satoshi, T. Wakana, K. Yoichi, S. Norimasa, S. Toshiaki, PIV measurement of carbon dioxide gas-liquid two-phase nozzle flow, ASME Proceedings: Symposium on Noninvasive Measurements in Single and Multiphase Flows, 2015.
[11] F. Scarano, M.L. Riethmuller, Iterative multigrid approach in PIV image processing with discrete window offset, Exp. Fluids 26 (6) (1999) 513–523.
[12] F. Scarano, M.L. Riethmuller, Advances in iterative multigrid PIV image processing, Exp. Fluids 29 (1) (2000) S051–S060.
[13] T. van der Stelt, N.R. Nannan, P. Colonna, The iPRSV equation of state, Fluid Phase Equilib. 330 (2012) 24–35.
[14] V. Valori, Rayleigh-Benard convection of a supercritical fluid: (PIV) and heat transfer study, [PhD thesis] Delft University of Technology, 2017.
[15] E.L. Warrick, The application of bond refractions to organo-silicon chemistry, J. Am. Chem. Soc. 68 (12) (1946) 2455–2459.
[16] J. Westerweel, F. Scarano, Universal outlier detection for PIV data, Exp. Fluids 39 (6) (2005) 1096–1100.
[17] B. Wieneke, PIV uncertainty quantification from correlation statistics, Meas. Sci. Technol. 26 (7) (2015).
[18] C.E. Willert, M. Gharib, Digital particle image velocimetry, Exp. Fluids 10 (4) (1991) 181–193.